

Multi-View Fusion of Sensor Data for Improved Perception and Prediction in Autonomous Driving

Sudeep Fadadu*, Shreyash Pandey*, Darshan Hegde, Yi Shi,
Fang-Chieh Chou, Nemanja Djuric, Carlos Vallespi-Gonzalez

Uber Advanced Technologies Group

{sfadadu, shreyash, darshan.hegde, yishi, fchou, ndjuric, cvallespi}@uber.com

Abstract: We present an end-to-end method for object detection and trajectory prediction utilizing multi-view representations of LiDAR returns. Our method builds on a state-of-the-art Bird’s-Eye View (BEV) network that fuses voxelized features from a sequence of historical LiDAR data as well as rasterized high-definition map to perform detection and prediction tasks. We extend the BEV network with additional LiDAR Range-View (RV) features that use the raw LiDAR information in its native, non-quantized representation. The RV feature map is projected into BEV and fused with the BEV features computed from LiDAR and high-definition map. The fused features are then further processed to output the final detections and trajectories, within a single end-to-end trainable network. In addition, using this framework the RV fusion of LiDAR and camera is performed in a straightforward and computational efficient manner. The proposed approach improves the state-of-the-art on proprietary large-scale real-world data collected by a fleet of self-driving vehicles, as well as on the public nuScenes data set.

Keywords: self-driving cars, sensor fusion, object detection, motion prediction

1 INTRODUCTION

Self-driving vehicle (SDV) is a highly involved system, relying on several input sensors (such as LiDARs, radars, and cameras) to detect objects in its vicinity, as well as predict their future motion and the motion uncertainty [1]. These tasks are necessary for ensuring safe and efficient routing through a stochastic world, where deep learning approaches have proven to be very effective tools. In particular, a number of work has been recently proposed to address detection of traffic actors from sensor data [2, 3], as well as their motion prediction where detected objects are taken as inputs [4, 5]. Here, the two tasks are solved separately and in a sequence, with the detection and prediction models trained in isolation. However, such multi-stage systems may result in added system latency due to lack of feature sharing, and suffer from cascading errors. To address this issue, joint models performing the two tasks as a part of a single end-to-end system were proposed recently [6], where gradients can flow from output trajectories to detections and further back to the sensor data.

Most recent work on end-to-end models operates in the Bird’s-Eye View (BEV) [6, 7], projecting the raw LiDAR data into a top-down grid centered on the SDV. BEV encoding of LiDAR returns has several advantages in terms of making the object detection and motion forecasting task easier to learn. One such advantage is that the size of objects remains constant regardless of range, which provides a strong prior to the output space and simplifies the problem. Other advantages include effective fusion of historical LiDAR data, as well as efficient fusion of high-definition (HD) map features [7]. However, this representation discretizes the LiDAR data into voxels, losing fine-grained information that might be necessary to detect smaller objects such as pedestrians and bicyclists.

On the other hand, Range-View (RV) methods operate in LiDAR’s native, dense representation, providing full access to the non-quantized sensor information. This property has been shown to provide both efficiency benefits and strong detection performance, especially when it comes to smaller

*equal contribution

objects like pedestrians and bicyclists [2]. RV representation is also arguably better suited for efficiently fusing information from sensors that natively capture data in RV, like LiDAR and camera [3]. However, these approaches operate on RV inputs while outputting 3D detections in a BEV space, implying that the model needs to learn the transformation from RV to BEV. Moreover, such models also have to handle variations in perceived size of objects with range. These issues make the problem more complex, and the model thus requires a larger data set in order to be competitive with the BEV-based methods. Recently, methods such as [8] also showed that fusing historical LiDAR data in RV is challenging due to distortions that arise due to shift in the center of spherical projection.

In this work we propose a novel model that combines the benefits of BEV and RV methods under a unified framework. In particular, we introduce an improved data fusion scheme that projects LiDAR data into both BEV and RV representations, where it is combined with HD map data and camera, respectively. Then, the two views are processed separately before being fused in a common BEV frame, where joint detection and motion prediction is performed. We show that such multi-view LiDAR processing results in significant improvements over the baselines that only focus on single-view processing of each data source. In summary, the main contributions of our work are as follows:

- we propose multi-view encoding and processing of LiDAR data separately in BEV and RV frames, before fusing the two views in a common BEV feature space;
- we propose to perform early fusion of the camera data with LiDAR in the RV frame, before projecting the learned features to the BEV frame;
- we present an ablation study and compare the method to the state-of-the-art on proprietary and open-sourced data, indicating improvements in both detection and motion prediction.

2 RELATED WORK

Accurate 3D object detection using LiDAR point clouds is a key technology in SDV development. To apply deep neural networks on point cloud data, it needs to be converted into appropriate feature representations that can be ingested by the deep models. A popular approach is to treat the points as an unordered set of point-wise feature vectors, first proposed by PointNet [9], and applied to object detection in F-PointNet [10] and StarNet [11]. Another common method is to voxelize the point cloud onto BEV grid cells and apply CNN on the BEV feature map, as done in PIXOR for object detection [12]. HDNET [13] extends PIXOR with additional HD map inputs. VoxelNet [14] and PointPillar [15] use point-based feature extraction on each BEV grid cells before applying CNN. Lastly, LaserNet [2] proposes an RV representation of LiDAR points, by unwarping the cylindrical LiDAR sweep onto a 2D feature map, where each pixel represents features of a single LiDAR point.

Most of the detection methods, as discussed above, use only one feature representation of LiDAR. Some recent research explore the idea of combining multiple LiDAR feature representations, known as the Multi-View (MV) approach. MV3D [16] uses a BEV-based network to perform region proposal, applies Region of Interest (ROI) pooling on BEV, RV, and image feature map to extract 1D feature vector for each view, and fuses the 1D features of different views before the final detection heads. MVF [17] first voxelizes the point cloud in two different views: BEV and perspective view, extracts point-wise embedding in the two views separately to augment the point-wise feature, then applies PointPillar-style BEV network to generate detection. MVLidarNet [18] first performs semantic segmentation on RV representation of LiDAR points, projects the predicted segmentation class probability into BEV, and applies a second network to generate detection on BEV feature map. Each of the methods discussed above has certain weaknesses. MV3D uses a large network for each view and only performs late MV fusion after ROI cropping. MVF uses expensive additional networks to obtain point-wise embedding in multiple views before applying the backbone BEV network. MVLidarNet is computationally efficient, but it only fuses RV segmentation output to BEV, and gives inferior detection results than recent BEV detectors on KITTI [19]. In comparison, our proposed method extracts informative RV features with a lightweight network and fuses to existing state-of-the-art BEV architecture before the object detection is performed, which gives significant performance improvements at a small computation cost.

A related field of research is LiDAR-camera fusion in object detection. Camera images are natively presented in the 2D front view, distinct from the common BEV representation for LiDAR data. In addition, the camera images do not give direct depth measurements on each pixel, so one cannot trivially project the camera pixels onto BEV grids. AVOD [20] and MV3D [16] fuse camera and

LiDAR features after second-stage feature cropping. F-PointNet [10] applies 2D object detection method on the camera image, then uses PointNet on LiDAR points falling into the frustum of each 2D detection to generate 3D detections. Continuous fusion (ContFuse) [21] finds the nearest LiDAR points for each BEV grid cell, and projects these 3D points onto camera image to extract corresponding image features. PL++ [22] estimates depth of each camera pixel and treats it as a pseudo-LiDAR point, then corrects the depth estimation with sparse LiDAR inputs before applying standard 3D detection algorithms on the pseudo-LiDAR point cloud. MMF [23] combines several fusion ideas: it fuses camera features to BEV features at multiple scales using ContFuse, augments ContFuse with additional pseudo-LiDAR points from an image depth estimator, and performs second-stage fusion by concatenating feature map crops from BEV and camera view. Lastly, recently proposed LaserNet++ [24] extended LaserNet with image fusion. Since the RV feature in LaserNet is in the same front view as the camera image feature, LaserNet++ simply projects the camera feature onto the RV feature map, and the authors show improvements over previous state-of-the-art object detection and LiDAR segmentation algorithms at a small computational cost. In this paper we make use of LaserNet++ approach to fuse LiDAR and camera in RV, before combining the fused features with the BEV feature map.

In recent years, it became increasingly common to employ a single end-to-end trained model to jointly perform object detection and trajectory prediction, an approach introduced by the authors of FaF [25]. A follow-up work IntentNet [6] further uses map information and predicts both trajectories and actors’ high-level intents. SpaGNN [26] proposes a two-stage model where it crops the feature map for each actor with rotated ROI (RROI), and models actor interactions and uncertainties by a graph neural network (GNN). PnPNet [27] performs detection, prediction and tracking in one end-to-end network. LaserFlow [8] extends LaserNet with multi-sweep LiDAR inputs in RV and is able to perform both detection and prediction. STINet [28] proposes a spatial-temporal network that generates detection, future trajectory, and past locations for each pedestrian, and handles actor interactions with GNN. MultiXNet [7] extends IntentNet with second-stage trajectory refinement, joint detection and prediction on multiple classes of actors, and multi-modal trajectory prediction, and is able to achieve state-of-the-art results on the ATG4D data set. Our work builds on MultiXNet through additional multi-view and camera fusion, resulting in significant boost in performance.

3 PROPOSED APPROACH

In this section, we present our multi-view approach to jointly detect and forecast motion for multiple traffic actor types using raw sensor data: LiDAR point clouds, camera RGB images, and HD maps. We first describe the model inputs and then delve into network architecture and learning objective.

3.1 Input Representation

LiDAR Point Cloud: As discrete convolutions operate on grid-structured inputs, previous approaches proposed to convert the 3D point cloud into either a BEV grid or an RV grid. A BEV grid simplifies the problem of object detection due to preservation of metric space and size constancy. It also simplifies the problem of motion prediction due to effective and straightforward fusion of historical LiDAR data with HD map on the BEV grid, as shown by MultiXNet [7]. On the other hand, an RV grid preserves detailed information about smaller objects and allows efficient fusion of other RV sensors such as camera, as shown by [2] and [3]. Unlike the earlier work, our proposed method exploits both RV and BEV representations of LiDAR data.

We collect the LiDAR returns in sweeps, each containing data collected by the sensor in one full 360° rotation. We follow the same method as [7] to encode a history of LiDAR sweeps in a BEV grid. Each LiDAR sweep \mathcal{S}_t at time t comprises LiDAR points represented by their (x, y, z) locations. Then, sweep \mathcal{S}_t is voxelized in a BEV image centered on the SDV, with voxel sizes of Δ_L , Δ_W , and Δ_V along the x -, y -, and z -axes, respectively. Each voxel encodes binary occupancy indicating whether there exists at least one LiDAR point in that voxel. With this setting, the input feature for each sweep \mathcal{S}_t is of shape $\left\lceil \frac{L}{\Delta_L} \right\rceil \times \left\lceil \frac{W}{\Delta_W} \right\rceil \times T \left\lceil \frac{V}{\Delta_V} \right\rceil$, where length L , width W , and height V define the area of interest in a 3D physical space around the SDV. We also encode the $T - 1$ past sweeps $\{\mathcal{S}_{t-T+1}, \dots, \mathcal{S}_{t-1}\}$ into the same BEV frame, and stack the feature maps along the channel dimension.

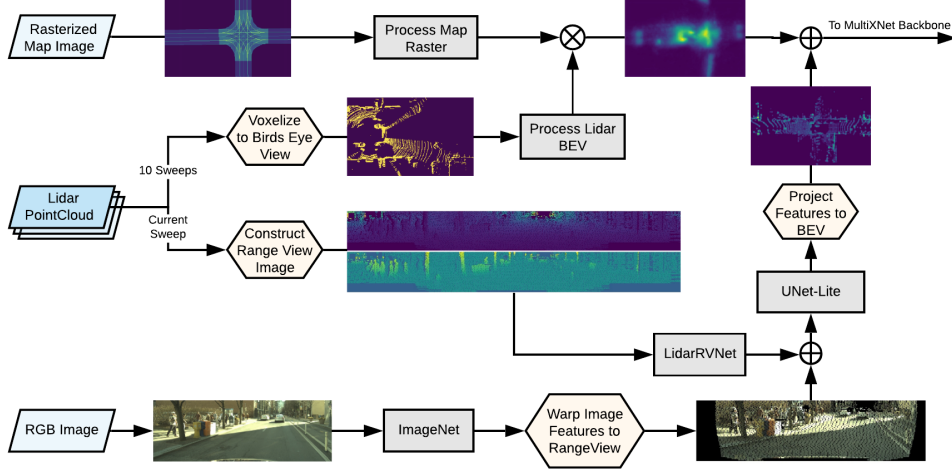


Figure 1: Overview of the proposed multi-view sensor fusion architecture.

For RV representation of the LiDAR sweep we follow the approach from [2]. Each LiDAR point is described by range r , intensity e , azimuth θ , and laser ID m , which maps to a known elevation angle of the corresponding laser beam. The input RV image is generated by converting laser ID m into rows and discretizing azimuth θ into columns, covering a full 360° view around the SDV. We pick the horizontal resolution of the RV image such that all sensor readings fall into different pixels. Each image pixel contains four channels: range r , height from the ground z , intensity e , and a binary value indicating whether the cell contains a valid sensor reading (for invalid sensor readings we set values of the other three channels to -1). In this paper we only embed the current LiDAR sweep \mathcal{S}_t in RV, while past sweeps are only used in the BEV embedding described above.

High-Definition Map: Similarly to [7], we form a BEV representation of an HD map by rasterization. Specifically, we encode static map elements in the same frame as our BEV LiDAR grid. Static map elements include driving paths, crosswalks, lane and road boundaries, intersections, driveways, and parking lots, where each element is encoded as a binary mask in its own separate channel. This results in a total of seven map channels used as a model input, shown in the top part of Figure 1.

Camera Image: We use the current RGB image frame from front camera as an additional input. It is expected for camera to help with object detection at longer ranges, where LiDAR data is sparse.

3.2 Network Architecture

In this section we introduce the proposed multi-view architecture, illustrated in Figure 1. Our architecture is composed of two major parts, feature extractors and feature projectors. We first explain feature projector logic, and then explain how projection is used along with the feature extractor that is tasked with processing and fusing different views.

3.2.1 Point-based Feature Projection

To project features from one view to another we use a simple, generic method, described below. In our proposed approach we use three views: camera view, LiDAR RV, and BEV. The projection between these views is computed as follows,

$$F_{target}(x) = \frac{\sum_{i=1}^N 1_{x=\mathcal{P}_{target}(L_i)} F_{source}(\mathcal{P}_{source}(L_i))}{\sum_{i=1}^N 1_{x=\mathcal{P}_{target}(L_i)}}. \quad (1)$$

Here F_{target} and F_{source} are feature maps in the target and source views, respectively, represented as 2D grids and indexed by a cell index, while x denotes a cell index within the target grid. \mathcal{P}_{target} and \mathcal{P}_{source} are projection operators that project LiDAR point L_i onto the corresponding view and return the cell index in that view. Scalar N is the total number of LiDAR points in a sweep, while

1_c is an indicator function which equals 1 when condition c is true and 0 otherwise. In other words, we use LiDAR points to extract features from the source view and project them into the target view, then apply average pooling if multiple LiDAR points are projected into the same target cell.

3.2.2 Multi-view Fusion

Our multi-view model takes in two branches of LiDAR inputs, one for BEV inputs and another for RV inputs. In the following, we refer to them as BEV branch and RV branch for simplicity.

BEV Branch: The BEV branch is similar to MultiXNet [7], where we separately extract features from voxelized multi-sweep LiDAR data on one side and rasterized HD map on the other. The two sets of features are then summed, before being sent downstream to MultiXNet first-stage backbone network explained in the following section.

RV Branch: The RV branch consumes LiDAR point-cloud data and RGB camera images, and fuses them in the RV before projection onto BEV. The RV camera fusion is inspired by prior work [3], which showed that fusion of camera features with the RV LiDAR features is both efficient and effective. This can be explained by two reasons:

- (i) Distortion from the projection of camera features from camera view to RV LiDAR frame has less severe consequences than direct projection to BEV. While small calibration or synchronization errors may result in large BEV projection errors (especially at the object boundaries), the RV projection errors result in shifts of only a few pixels, making them easily recoverable even with small networks.
- (ii) As the projection distortion is minimal and recoverable, LiDAR and camera RV features can be fused early and share most of the feature processing, resulting in greater efficiency.

Next we discuss the RV branch in detail. We first construct the RV image from LiDAR point cloud, which is then processed by 2 convolutional layers with 3×3 kernel without stride. In parallel, we extract features from RGB camera image with a lightweight *ImageNet*, which consists of 6 layers of convolutions, each with 3×3 kernel and stride 2 for every alternate layer. We project these extracted camera features to LiDAR RV using Equation (1), then concatenate them with the LiDAR RV features along with a binary indicator encoding whether the RV cell contains a valid camera projection (we use 1 and -1 to indicate valid and invalid projection, respectively). Next, we apply a multi-scale U-Net [29] on the concatenated features. Our U-Net architecture processes the features at 2 scales, each down-scaling 2x horizontally and double the channel size. We use a residual block with skip connection as a processing block at each level, followed by a deconv layer for feature upsampling. Lastly, the resulting RV features are projected into BEV using Equation (1).

3.2.3 Backbone Network and Loss Function

The rest of the model processing is performed in BEV frame, following a two-stage architecture proposed by MultiXNet [7]. In the first stage the model outputs a detection for each grid cell, outputting existence probability \hat{p} , bounding box center $(\hat{c}_{x0}, \hat{c}_{y0})$, length \hat{l} and width \hat{w} of the bounding box, and heading $\hat{\theta}_0$. The trajectory prediction comprises waypoint centers $(\hat{c}_{xh}, \hat{c}_{yh})$ and headings $\hat{\theta}_h$ at future time horizon h . Bounding box shape is considered constant across the prediction horizon.

We define foreground cells (fg) as cells containing labeled objects. Then, loss function at prediction horizon h computed at such cells is defined as follows,

$$\begin{aligned} \mathcal{L}_{fg(h)} = & 1_{h=0} \left(\ell_{focal}(\hat{p}) + \ell_1(\hat{l} - l) + \ell_1(\hat{w} - w) \right) + \\ & \ell_1(\hat{c}_{xh} - c_{xh}) + \ell_1(\hat{c}_{yh} - c_{yh}) + \ell_1(\sin \hat{\theta}_h - \sin \theta_h) + \ell_1(\cos \hat{\theta}_h - \cos \theta_h). \end{aligned} \quad (2)$$

Here $\ell_{focal}(\hat{p}) = (1 - \hat{p})^\gamma \log \hat{p}$ is a focal loss [30] with $\gamma = 2$, and ℓ_1 is the smooth- ℓ_1 regression loss. Values l, w, c_{xh}, c_{yh} , and θ_h are ground-truth values. For cells without labeled objects called background cells (bg), the loss is $\mathcal{L}_{bg} = \ell_{focal}(1 - \hat{p})$. Then, the overall first-stage loss equals

$$\mathcal{L} = 1_{bg \text{ cell}} \mathcal{L}_{bg} + 1_{fg \text{ cell}} \sum_{h=0}^H \lambda^h \mathcal{L}_{fg(h)}, \quad (3)$$

where $\lambda \in (0, 1)$ is a constant decay factor (set to 0.97 in our experiments).

In addition, we also model uncertainty of each waypoint, refine the trajectories for vehicles with a second-stage rotated region-of-interest cropping, and output multi-modal trajectory predictions for vehicle actors. We refer the reader to [7] for details, which are skipped here due to lack of space. The final output of the model contains the detection bounding boxes and trajectory predictions for all three main classes of road actors, namely vehicles, pedestrians, and bicyclists.

4 EXPERIMENTS

4.1 Data sets

We evaluate our method on two autonomous driving data sets, ATG4D and nuScenes [31]. ATG4D is a proprietary data set collected using a 64-beam LiDAR with 10Hz sweep capture frequency, and a front camera capturing images at 1920×1200 resolution with a horizontal field of view (FOV) of 90° . The data contains over 1 million frames from 5,500 different scenes, with tracked 3D bounding box labels at maximal range of 100m. nuScenes is a publicly available data set that uses a 32-beam LiDAR with 20Hz sweep capture frequency, a front camera with 1600×900 resolution and a horizontal FOV of 70° . The data contains 1,000 scenes with 390,000 LiDAR sweeps.

For ATG4D, we evaluate using the same setting as MultiXNet [7]. The BEV input uses $L = 150\text{m}$, $W = 100\text{m}$, $V = 3.2\text{m}$, $\Delta_L = 0.16\text{m}$, $\Delta_W = 0.16\text{m}$, $\Delta_V = 0.2\text{m}$, and we use $T = 10$ sweeps to predict $H = 30$ future states at 10Hz (thus using 1s of history to predict 3s into future). The RV input only uses the current LiDAR sweep, with an input resolution of 2048×64 . We use the front camera RGB image synchronized with the current LiDAR sweep, after cropping 438 pixels from the top which mostly include sky.

For nuScenes, we use same hyper-parameters and loss functions as in the ATG4D experiment, with a few changes in input representations. The BEV input uses $L = 100\text{m}$, $W = 100\text{m}$, $V = 8\text{m}$, $\Delta_L = 0.125\text{m}$, $\Delta_W = 0.125\text{m}$, $\Delta_V = 0.2\text{m}$, and we use $T = 10$ sweeps at 20Hz to predict $H = 30$ future states at 10Hz (thus using 0.5s of history to predict 3s into future). The RV input dimension is set to 2048×32 (note that there are less rows than for ATG4D as nuScenes uses 32-beam LiDAR). Camera images are used directly without cropping.

4.2 Experiment settings

In this section, we describe the experiments performed to evaluate our approach. We refer to our MV method as LC-MV when using both LiDAR and camera as inputs, and L-MV when only using lidar inputs where the camera sub-branch from Figure 1 is removed. We also consider MultiXNet baseline, which follows the exact implementation described in [7], as well as recently proposed Continuous Fusion method [21].

Continuous Fusion (ContFuse): To better evaluate the effect of MV camera fusion, we implemented a popular BEV-based camera fusion baseline that does not utilize MV for camera fusion. In particular, we apply continuous fusion [21] to project camera feature to BEV and fuse it with the MultiXNet backbone. Continuous fusion projects the camera feature into a dense BEV feature map. For each target BEV pixel, it finds the nearest K LiDAR points within distance d and projects the LiDAR points onto the camera feature map to retrieve the corresponding image features. The image features are concatenated with geometry information and fed into multi-layer perceptron (MLP) to output the per-pixel feature in BEV. We extracted camera features of dimension size 32 from ResNet-34 [32] backbone with an extra Feature Pyramid Module [33]. We set the number of neighbors $K = 1$ and distance $d = 3\text{m}$. The 3D offsets between the source LiDAR point and the target BEV pixel are used as additional geometry information. A 3-layer MLP with hidden layer of size 128 is used for feature extraction. The projected camera BEV features is added to the LiDAR+map BEV features, at the same layer as in our proposed architecture shown in Figure 1.

We evaluated the methods using both detection and prediction metrics, following the same setting as in [7]. We report the Average Precision (AP) detection metric, with IoU threshold set to 0.7, 0.1, 0.3 for vehicles, pedestrians, and bicyclists, respectively. For prediction metrics we use Displacement Error (DE) [34] at 3s, where the detection probability threshold resulting in a recall of 0.8 is used as the operational point. Model inference latency is computed on RTX 2080Ti with TensorRT optimization. Since we only use the front camera which captures a fragment of the full 360° area around SDV, in Tables 1 and 2 we also report the detection results that only include actors appearing

Table 1: Evaluation on nuScenes using detection AP (%), prediction DE (cm), and latency (ms)

Method	Vehicles					Pedestrians					Bicyclists					
	AP _{0.7} ↑				DE↓	AP _{0.3} ↑				DE↓	AP _{0.1} ↑				Lat.↓	
	Full	In Camera FOV				Full	In Camera FOV				Full	In Camera FOV				
		0m-50m	0m-25m	25m-50m			0m-50m	0m-25m	25m-50m			0m-50m	0m-25m	25m-50m		
MultiXNet	60.6	60.9	80.0	43.3	108.2	65.5	63.8	72.9	54.1	86.5	31.7	32.1	41.4	25.2	191.3	32.3
ContFuse	60.9	61.9	79.4	46.0	109.6	67.2	71.6	78.0	64.3	82.4	33.5	44.1	53.5	36.1	187.9	63.6
L-MV	61.1	61.5	79.6	45.3	107.2	71.0	70.4	79.1	60.6	82.3	38.2	38.1	53.3	25.8	187.3	37.4
LC-MV	62.9	63.3	81.2	47.0	106.5	71.4	73.1	80.4	64.6	80.0	39.8	40.4	53.6	29.5	178.8	38.3

Table 2: Evaluation on ATG4D using detection AP (%), prediction DE (cm), and latency (ms)

Method	Vehicles										Pedestrians										Bicyclists												
	AP _{0.7} ↑										DE↓	AP _{0.1} ↑										DE↓	AP _{0.3} ↑										Lat.↓
	Full	In Camera FOV					Full	In Camera FOV					Full	In Camera FOV					Full	In Camera FOV													
		0m-75m	0m-25m	25m-50m	50m-75m			0m-75m	0m-25m	25m-50m	50m-75m			0m-75m	0m-25m	25m-50m	50m-75m			0m-75m	0m-25m	25m-50m	50m-75m			0m-75m	0m-25m	25m-50m	50m-75m				
MultiXNet	84.2	83.9	92.6	85.5	68.6	80.2	88.6	88.9	87.3	89.5	88.0	57.1	84.6	82.2	87.4	78.7	76.8	48.6	35.2														
LC-MV	84.7	84.5	92.6	86.1	70.1	78.7	89.4	89.8	88.5	90.1	88.7	56.5	87.3	85.2	90.8	81.5	76.8	49.4	43.4														

in camera FOV. Note that nuScenes [31] recommends a different AP definition using thresholds on 2D center distances instead of IoUs between detection and ground-truth, and has finer class types on vehicles (cars, buses, trucks, etc.). Here we use the standard IoU-based AP and aggregate all vehicle actor types into one class, to obtain a consistent metric definition across the data sets. As a result, our reported results on nuScenes are not directly comparable to other published works.

4.3 Results

Table 1 presents model evaluation results on the public nuScenes data set. Note that the bicyclists is one of the rarest class types in nuScenes, therefore its detection AP is significantly lower than that of the other classes. This is however aligned with the results reported in [31]. When compared to the MultiXNet baseline, our LiDAR-only MV method already gives significantly improved detection AP for all three actor classes, resulting in 0.5% improvement for vehicles, 5.5% for pedestrians, and 6.5% for bicyclists, as well as better prediction errors. Including camera input in the MV fusion gives further improvements in both detection and prediction metrics. In comparison, we can see that the ContFuse baseline, while showing notable improvements over the MultiXNet baseline, performs worse when compared to the proposed LC-MV fusion model in overall metrics across all actor types.

To further understand the effect of camera fusion, Table 1 also includes detection metrics within the camera FOV, with further metrics slicing based on the actor distance to SDV in meters. As expected, the metrics gains between L-MV and LC-MV are more pronounced within the camera FOV, as opposed to the overall metrics across the full 360° view. With further distance-based metrics slicing, we found that the MV fusion in general shows similar or larger improvements at longer ranges. This is most evident for vehicle actors, yielding 0.3% improvement in near range and 6% improvement at long range when comparing MultiXNet to LC-MV model. The result is aligned with findings by previously reported results on RV-based detectors [2, 3], indicating that the RV representation is more effective in capturing longer-range objects. We also note better AP results by ContFuse for bicyclists in the camera FOV, especially at long range. We hypothesize that this category might have benefited from deeper image-processing network used by ContFuse. Nevertheless, our method performs significantly better in the overall metrics with much lower latency, discussed further below.

Table 2 shows the model evaluation metrics on ATG4D, which has higher-resolution sensors, longer detection range, and larger data size than nuScenes. We can see that the proposed model is able to improve the detection AP over MultiXNet across all three actor types. As in the nuScenes comparison, for smaller object types (i.e., pedestrians and bicyclists) the method shows the largest improvements. On the trajectory prediction task, our MV model also improves the vehicle and pedestrian motion prediction, while slightly regressing on bicyclist actors.

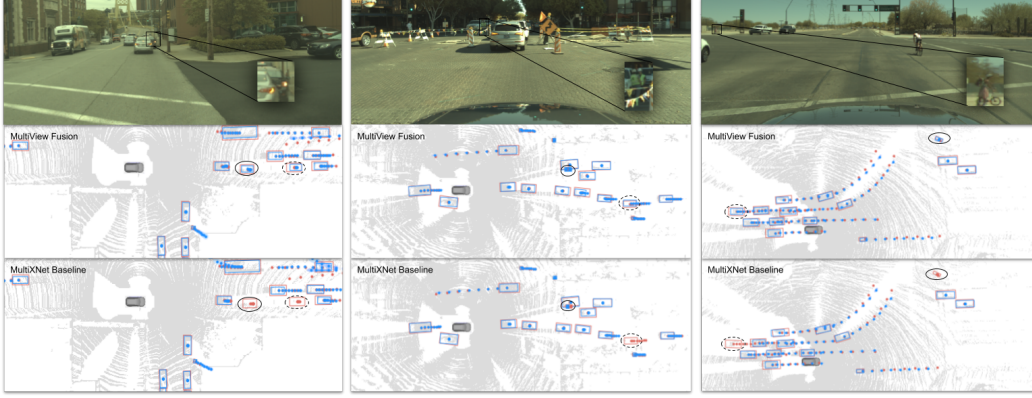


Figure 2: Qualitative comparison of the proposed model (middle row) and MultiXNet (bottom row); model predictions are shown in blue and ground truth is shown in red

The model inference latency on nuScenes is presented in Table 1. We can see that adding MV LiDAR fusion results in additional 5ms inference time over the MultiXNet baseline. Including the front camera in our architecture is computationally inexpensive, since we use a lightweight image-processing network, which only adds an additional 1ms. In comparison, adding camera input to MultiXNet through ContFuse increases the latency by 31ms, much larger slowdown than by using the proposed LC-MV model. The results demonstrate that our proposed architecture is highly efficient, both within the MV fusion architecture and the image-processing network. As a result, the method can easily be scaled to use multiple cameras (e.g., side and rear cameras) while maintaining real-time inference speed. On ATG4D, which uses higher-resolution camera, denser LiDAR inputs, as well as larger BEV region of interest, our method has a latency of 43ms (as shown in Table 2), which is well within the real-time requirement of typical SDV applications.

Lastly, we present several qualitative examples illustrating how the introduced fusion method improves object detection of traffic actors in the ATG4D data set. Figure 2 shows three examples where the MultiXNet baseline fails to detect actors at longer distances while having a clear view in the camera image (shown as solid circles in BEV). In all three cases our proposed method is able to reliably detect the far-away actors, which include all three actor types of interest (vehicle, pedestrian, and bicyclist, respectively). The LC-MV model also detects several additional actors missed by MultiXNet, which are shown as dotted circles. We can see that the trajectory predictions for the additional detected actors are also accurate compared to the ground truth, exemplifying good performance of the proposed approach in terms of both object detection and motion prediction.

5 CONCLUSION

In this paper we focused on object detection and motion prediction of traffic actors, which are safety-critical problems in the development and deployment of SDVs. While there is a significant amount of published work that treats these tasks in isolation, recent research has shown that end-to-end methods performing detection and prediction jointly achieve state-of-the-art performance. The end-to-end approaches can be roughly grouped into BEV-based and RV-based, depending on how the input data is encoded and processed. We recognized the advantages and disadvantages of both methods, and proposed a novel multi-view model that combines the best of both groups in a unified architecture. In particular, we proposed to combine LiDAR points with camera data in the RV and with the map in BEV, before fusing the view-specific features in a common BEV frame. This allows improved processing on sensor data resulting in better performance of the overall system and small increase in overall latency. We evaluated the proposed approach on large-scale, real-world autonomous driving data sets, and compared to the state-of-the-art end-to-end approaches. The results indicate that the novel fusion method outperforms the baselines along both detection and prediction metrics, strongly suggesting practical benefits of the proposed multi-view fusion approach. Moreover, while we applied the proposed multi-view method to MultiXNet, we emphasize that the proposed method is very general and is directly applicable to other BEV algorithms, where it can be used to improve object detection and motion prediction performance.

Acknowledgments

References

- [1] J. Ziegler, P. Bender, M. Schreiber, et al. Making bertha drive—an autonomous journey on a historic route. *IEEE Intelligent Transportation Systems Magazine*, 6:8–20, 10 2015.
- [2] G. P. Meyer, A. Laddha, E. Kee, C. Vallespi-Gonzalez, and C. K. Wellington. Lasernet: An efficient probabilistic 3d object detector for autonomous driving. In *Proceedings of the IEEE Conference on Computer Vision and Pattern Recognition*, pages 12677–12686, 2019.
- [3] G. P. Meyer, J. Charland, D. Hegde, A. Laddha, and C. Vallespi-Gonzalez. Sensor fusion for joint 3d object detection and semantic segmentation. In *The IEEE Conference on Computer Vision and Pattern Recognition (CVPR) Workshops*, June 2019.
- [4] N. Djuric, V. Radosavljevic, H. Cui, T. Nguyen, F.-C. Chou, T.-H. Lin, and J. Schneider. Uncertainty-aware short-term motion prediction of traffic actors for autonomous driving. In *IEEE Winter Conference on Applications of Computer Vision (WACV)*, 2020.
- [5] H. Cui, V. Radosavljevic, F.-C. Chou, T.-H. Lin, T. Nguyen, T.-K. Huang, J. Schneider, and N. Djuric. Multimodal trajectory predictions for autonomous driving using deep convolutional networks. In *2019 International Conference on Robotics and Automation (ICRA)*, pages 2090–2096. IEEE, 2019.
- [6] S. Casas, W. Luo, and R. Urtasun. Intentnet: Learning to predict intention from raw sensor data. In *Conference on Robot Learning*, pages 947–956, 2018.
- [7] N. Djuric, H. Cui, Z. Su, S. Wu, H. Wang, F.-C. Chou, L. S. Martin, S. Feng, R. Hu, Y. Xu, et al. Multixnet: Multiclass multistage multimodal motion prediction. *arXiv preprint arXiv:2006.02000*, 2020.
- [8] G. P. Meyer, J. Charland, S. Pandey, A. Laddha, C. Vallespi-Gonzalez, and C. K. Wellington. Laserflow: Efficient and probabilistic object detection and motion forecasting. *arXiv preprint arXiv:2003.05982*, 2020.
- [9] R. Q. Charles, H. Su, M. Kaichun, and L. J. Guibas. Pointnet: Deep learning on point sets for 3d classification and segmentation. *2017 IEEE Conference on Computer Vision and Pattern Recognition (CVPR)*, Jul 2017. doi:10.1109/cvpr.2017.16. URL <http://dx.doi.org/10.1109/CVPR.2017.16>.
- [10] C. R. Qi, W. Liu, C. Wu, H. Su, and L. J. Guibas. Frustum pointnets for 3d object detection from rgb-d data. In *Proceedings of the IEEE conference on computer vision and pattern recognition*, pages 918–927, 2018.
- [11] J. Ngiam, B. Caine, W. Han, B. Yang, Y. Chai, P. Sun, Y. Zhou, X. Yi, O. Alsharif, P. Nguyen, et al. Starnet: Targeted computation for object detection in point clouds. *arXiv preprint arXiv:1908.11069*, 2019.
- [12] B. Yang, W. Luo, and R. Urtasun. Pixor: Real-time 3d object detection from point clouds. In *Proceedings of the IEEE conference on Computer Vision and Pattern Recognition*, pages 7652–7660, 2018.
- [13] B. Yang, M. Liang, and R. Urtasun. Hdnet: Exploiting hd maps for 3d object detection. In *Conference on Robot Learning*, volume 87, pages 146–155, 2018.
- [14] Y. Zhou and O. Tuzel. Voxelnet: End-to-end learning for point cloud based 3d object detection. In *Proceedings of the IEEE Conference on Computer Vision and Pattern Recognition*, pages 4490–4499, 2018.
- [15] A. H. Lang, S. Vora, H. Caesar, L. Zhou, J. Yang, and O. Beijbom. Pointpillars: Fast encoders for object detection from point clouds. In *Proceedings of the IEEE Conference on Computer Vision and Pattern Recognition*, pages 12697–12705, 2019.
- [16] X. Chen, H. Ma, J. Wan, B. Li, and T. Xia. Multi-view 3d object detection network for autonomous driving. In *Proceedings of the IEEE Conference on Computer Vision and Pattern Recognition*, pages 1907–1915, 2017.
- [17] Y. Zhou, P. Sun, Y. Zhang, D. Anguelov, J. Gao, T. Ouyang, J. Guo, J. Ngiam, and V. Vasudevan. End-to-end multi-view fusion for 3d object detection in lidar point clouds. *arXiv preprint arXiv:1910.06528*, 2019.

- [18] K. Chen, R. Oldja, N. Smolyanskiy, S. Birchfield, A. Popov, D. Wehr, I. Eden, and J. Pehserl. Mvlidarnet: Real-time multi-class scene understanding for autonomous driving using multiple views. *arXiv preprint arXiv:2006.05518*, 2020.
- [19] A. Geiger, P. Lenz, and R. Urtasun. Are we ready for autonomous driving? the kitti vision benchmark suite. In *2012 IEEE Conference on Computer Vision and Pattern Recognition*, pages 3354–3361. IEEE, 2012.
- [20] J. Ku, M. Mozifian, J. Lee, A. Harakeh, and S. L. Waslander. Joint 3d proposal generation and object detection from view aggregation. In *2018 IEEE/RSJ International Conference on Intelligent Robots and Systems (IROS)*, pages 1–8. IEEE, 2018.
- [21] M. Liang, B. Yang, S. Wang, and R. Urtasun. Deep continuous fusion for multi-sensor 3d object detection. In *Proceedings of the European Conference on Computer Vision (ECCV)*, pages 641–656, 2018.
- [22] Y. You, Y. Wang, W.-L. Chao, D. Garg, G. Pleiss, B. Hariharan, M. Campbell, and K. Q. Weinberger. Pseudo-lidar++: Accurate depth for 3d object detection in autonomous driving. In *International Conference on Learning Representations*, 2019.
- [23] M. Liang, B. Yang, Y. Chen, R. Hu, and R. Urtasun. Multi-task multi-sensor fusion for 3d object detection. In *Proceedings of the IEEE Conference on Computer Vision and Pattern Recognition*, pages 7345–7353, 2019.
- [24] G. P. Meyer, J. Charland, D. Hegde, A. Laddha, and C. Vallespi-Gonzalez. Sensor fusion for joint 3d object detection and semantic segmentation. In *Proceedings of the IEEE Conference on Computer Vision and Pattern Recognition Workshops*, pages 0–0, 2019.
- [25] W. Luo, B. Yang, and R. Urtasun. Fast and furious: Real time end-to-end 3d detection, tracking and motion forecasting with a single convolutional net. In *Proceedings of the IEEE CVPR*, pages 3569–3577, 2018.
- [26] S. Casas, C. Gulino, R. Liao, and R. Urtasun. Spatially-aware graph neural networks for relational behavior forecasting from sensor data. *arXiv preprint arXiv:1910.08233*, 2019.
- [27] M. Liang, B. Yang, W. Zeng, Y. Chen, R. Hu, S. Casas, and R. Urtasun. Pnpnet: End-to-end perception and prediction with tracking in the loop. In *Proceedings of the IEEE/CVF Conference on Computer Vision and Pattern Recognition*, pages 11553–11562, 2020.
- [28] Z. Zhang, J. Gao, J. Mao, Y. Liu, D. Anguelov, and C. Li. Stinet: Spatio-temporal-interactive network for pedestrian detection and trajectory prediction. In *Proceedings of the IEEE/CVF Conference on Computer Vision and Pattern Recognition*, pages 11346–11355, 2020.
- [29] O. Ronneberger, P. Fischer, and T. Brox. U-net: Convolutional networks for biomedical image segmentation. In *International Conference on Medical image computing and computer-assisted intervention*, pages 234–241. Springer, 2015.
- [30] T.-Y. Lin, P. Goyal, R. Girshick, K. He, and P. Dollar. Focal loss for dense object detection. In *ICCV*, 2017.
- [31] H. Caesar, V. Bankiti, A. H. Lang, S. Vora, V. E. Liong, Q. Xu, A. Krishnan, Y. Pan, G. Baldan, and O. Beijbom. nuscenes: A multimodal dataset for autonomous driving. In *Proceedings of the IEEE/CVF Conference on Computer Vision and Pattern Recognition*, pages 11621–11631, 2020.
- [32] K. He, X. Zhang, S. Ren, and J. Sun. Deep residual learning for image recognition. In *Proceedings of the IEEE conference on computer vision and pattern recognition*, pages 770–778, 2016.
- [33] T. Lin, P. Dollár, R. B. Girshick, K. He, B. Hariharan, and S. J. Belongie. Feature pyramid networks for object detection. *CoRR*, abs/1612.03144, 2016. URL <http://arxiv.org/abs/1612.03144>.
- [34] A. Alahi, K. Goel, V. Ramanathan, A. Robicquet, L. Fei-Fei, and S. Savarese. Social lstm: Human trajectory prediction in crowded spaces. In *Proceedings of the IEEE conference on computer vision and pattern recognition*, pages 961–971, 2016.